nature communications

Article

https://doi.org/10.1038/s41467-026-68762-0

The contribution of sea-ice recrystallization to the Arctic snowpack

Received: 25 February 2025

Accepted: 15 January 2026

Published online: 06 February 2026

Check for updates

Amy R. Macfarlane[1,2,3] ✉, Moein Mellat[4], Ruzica Dadic[1,5], Hanno Meyer[4], Martin Werner[6], Camilla F. Brunello[6], Mahdi Jafari[1], Nander Wever[1], Stefanie Arndt[6,7], Daniela Krampe[6], Matthew Sturm[8] & Martin Schneebeli[1]

Understanding snow processes in the sea-ice system is essential to improving Arctic sea-ice predictions and climate modeling. We show that the winter snow cover on Arctic sea ice is strongly enriched in heavy isotopes near the snow-sea ice interface, unexplainable by snow metamorphism alone. During the MOSAiC expedition, stratigraphic investigations revealed that large temperature gradients drive water vapor transport and mass transfer from sea ice into the snowpack. We estimate the contributed snow depth equivalent as 39 ± 7 mm (cumulative mass redistribution) and 63 ± 21 mm (isotope two-source model). Despite uncertainties, both highlight the need for detailed snowpack vapor flux modeling. Recognizing this recrystallization process improves understanding of snow stratigraphy, gas exchange, atmospheric chemistry through snow impurity distributions (e.g., sea salt aerosol), and reduces uncertainties in snow mass balance and heat conductivity. With continued Arctic change, evolving snowpack temperature gradients and recrystallized sea-ice snow contributions will further shape these processes.

Snow on sea ice is the critical interface between the atmosphere and underlying ice, playing a crucial role in the sea-ice system's energy fluxes[1]. Accurate measurements and understanding of internal snowpack processes are essential, yet the remoteness of most Arctic sea-ice regions limits data collection and knowledge of these processes. Snow on sea ice is exposed to large temperature gradients (ΔT) due to the cold atmosphere and the relatively warmer ice-ocean interface, sustained by oceanic heat flux. These temperature gradients drive water vapor transport and mass flux within the snowpack, leading to substantial internal snow recrystallization through metamorphic processes that reorganize the snow crystals into new structures. This is known as temperature gradient metamorphism (TGM)[2–4], and a metamorphosed snow grain type, called depth hoar, accounts for 20–50% of the Arctic snowpack[5–8].

Internal snowpack water vapor transport is known to occur through both diffusion and convection; however, the contribution of the latter remains in discussion[9–12]. This is due to the dependency of convection on the snow density (ice volume fraction) remaining small enough to trigger convection circulation in the air pockets[13]. Complicating matters further, there is no definitive answer to the value of the vapor diffusion coefficient in snow[14,15]. Therefore, modeling and quantifying this vapor transport in the snowpack is complex but essential for understanding internal snow metamorphism and stratigraphy evolution[16].

The central Arctic snowpack is heavily influenced by i) wind redistribution, which erodes and deposits the snow[17,18] and ii) wind compaction, densifying the upper snowpack. These windy conditions prevent the preservation of atmospheric snow precipitation events in the snowpack stratigraphy, unlike a layered snowpack commonly

[1]WSL Institute for Snow and Avalanche Research SLF, Davos, Switzerland. [2]UiT The Arctic University of Norway, Tromsø, Norway. [3]Northumbria University, Newcastle upon Tyne, UK. [4]Alfred Wegener Institute Helmholtz Centre for Polar and Marine Research, Potsdam, Germany. [5]Victoria University of Wellington, Wellington, New Zealand. [6]Alfred Wegener Institute Helmholtz Centre for Polar and Marine Research, Bremerhaven, Germany. [7]University of Hamburg, Institute of Oceanography, Hamburg, Germany. [8]Geophysical Institute, University of Alaska Fairbanks, Fairbanks, AK, USA.
✉e-mail: amyrmacfarlane@gmail.com

https://doi.org/10.1038/s41467-026-68762-0

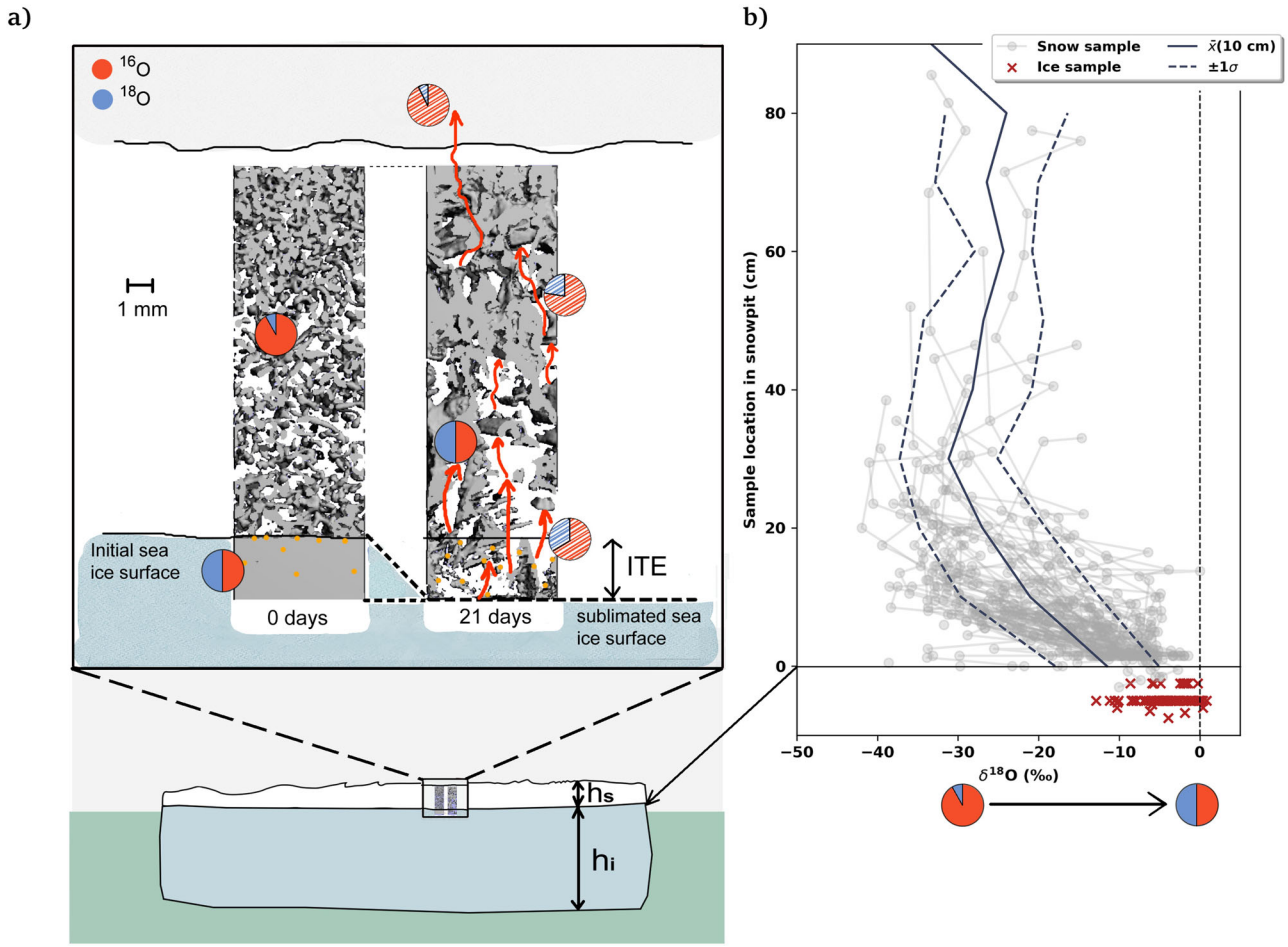

Fig. 1 | Conceptual model of sea ice sublimation and the isotopic two-source mixing model leading to ^{18}O enrichment of the lower snowpack. a The upper image shows an annotated microCT sample that highlights the processes of mass redistribution from the substrate into the snow from a previous lab experiment, where the underlying ice lens is now representing a sea-ice substrate. This microCT sample was first published by Mareike Wiese[24]https://www.research-collection.ethz.ch/entities/publication/133e13d0-e64f-413a-9676-6b93893f66cf. We have obtained permission from the rights-holder for its use in this publication, and it is now licensed under a CC BY 4.0 license https://creativecommons.org/licenses/by/4.0/. The original blue background and original annotations have been removed, and all annotations on this figure are modifications. Ice thickness equivalent (ITE, mm) is the thickness of sublimation of the sea-ice surface over 21 days. The pie charts show the approximate ratio of ^{16}O (red) to ^{18}O (blue) of solid ice (block color) and vapor (dashed). The red arrows represent vapor fluxes. The lower figure shows a cross-section of sea ice, where h_s = snow height, h_i = ice thickness, not drawn to scale. **b** One point represents one winter snow sample. The solid and dotted lines are the average profile with one standard deviation (± 1σ). 0 cm = snow-ice interface. Samples > 30 cm are in ridged areas. The pie charts show the snow-ice interface ^{18}O enrichment.

found in the Alps. Typically, simplistic modeled Arctic snowpacks have upper wind-packed layers with low permeability composed of well-sintered rounded grains and lower metamorphosed depth-hoar layers. However, large spatial heterogeneity and correlation length scales of 20–40 m[19], make the in situ stratigraphy datasets challenging to interpret.

Results from fieldwork on sea ice during the 1997/98 SHEBA expedition measured the depth-hoar development in the lower part of the snowpack and hinted towards water vapor transport originating from the ice substrate, which could serve as a potential moisture source[5]. This mass flux had been previously proven during field measurements of snow above a soil substrate, where the vapor flux out of the soil into the snow was measured by trapping and weighing the moisture that accumulated under an impermeable sheet[20]. They found the flux averaged 2.6×10^{-7} kg m^{-2} s^{-1}. Similarly[9], measured an upward vapor flux of 2.8–3.5 $\times 10^{-7}$ kg m^{-2} s^{-1} from a soil substrate into the snowpack and ref. 4 suggested soil moisture contributes to ~5% of the snow-water equivalent (SWE).

Laboratory and modeling experiments have applied temperature gradients ($\Delta T > 50$ K m^{-1}) to shallow snowpacks, resulting in substantial structural transformations[13,21,22]. One study observed a snow mass turnover of 60% per day[14]. These temperature gradients can potentially drive mass from the ice substrate into the snow[23]. A controlled laboratory experiment measured the mass incorporation and microstructural changes in snow above an ice lens[24]. They exposed the snow to $\Delta T = 100$ K m^{-1} and observed the rate of the ice lens sublimation. The rate of ice mass flux from the sublimating ice lens into the snow in this laboratory setting was 1.2×10^{-6} kg m^{-2} s^{-1} [24]. Figure 1a, shows an annotated micro-computed tomography (microCT) image from these laboratory experiments alongside conceptual isotopic enrichment pie charts, which are explained later in the stable water isotope section. In this microCT image, we see the development of depth hoar after 21 days alongside the sublimation of the ice substrate. Under these conditions (−11 °C < snow-surface temperature (T_s) < −16 °C, snow-ice interface temperature (T_i) = −3 °C, snow height (h_s) = 100 mm), the downward movement of the ice lens over time (t, time in days) is given in Equation (1), where $z_{il} - z_{il,0}$ represents the thickness of sublimation of the sea-ice surface (ice thickness equivalent, ITE given in mm)[24]. The correlation coefficient and p value of this

relationship were 0.92 and 1.92×10^{-47}.

$$\mathrm{ITE} = z_{il} - z_{il,0} = 0.11t + 0.07 \quad (1)$$

Stable water isotopes (δ^2H and δ^{18}O) are geochemical tracers, elucidating the historical processes of snow, such as vapor origins, recrystallization, and atmospheric conditions, e.g., temperature[25,26]. Throughout this study, the ratio of the heavy to light isotopes is given as the deviation from Vienna Standard Mean Ocean Water (V-SMOW), as δ^2H and δ^{18}O in permil (‰).

We can learn from isotopic snow studies in tundra environments to understand the upward contribution of vapor from the snow's substrate[4], despite a substrate's physical, chemical, and biological characteristics influencing its thermal properties, composition, and interaction with the above snowpack.[27] found stable water isotopic enrichment in the basal snowpack directly above the soil substrate, implying an upward mass flux from the soil substrate. A schematic diagram of this isotopic enrichment is shown in Fig. 1a using pie charts to represent the ratio of heavy ^{18}O to light ^{16}O. A pie chart with an equal amount of ^{16}O and ^{18}O represents δ^{18}O = 0‰. It is important to note that phase transitions within the snow lead to fractionation processes in the snowpack's isotopic composition[28,29]. Accordingly, TGM can enrich the basal snow in δ^{18}O in the range of 2‰[30] to 5‰[31], with an equivalent deposition and depletion in δ^{18}O in the layer above[31], which then, in turn, goes on to be enriched by further TGM. This effect reduces the isotope variability over time[29,32]. However, if an isotopically different vapor source (like one from a sea-ice substrate) is diffused through a snowpack, the snow's isotopic composition is modified[4,33,34].

In summary, three factors suggest that sea-ice substrate contributes mass to the overlying snow: (i) the typically large temperature gradients in snow on sea ice, exceeding those in tundra environments, due to a relatively shallow snow depth, (ii) the abundant moisture supply from the ice substrate, and (iii) evidence from tundra studies indicating an upward moisture flux from the underlying soil substrate. However, until now, no mass quantification of sea-ice recrystallization, referred to in this study as recrystallized sea-ice snow, has been attempted for the central Arctic. In this study, we examined snow measurements on sea ice from November 2019 to May 2020 above 83 °N during the MOSAiC (Multidisciplinary Drifting Observatory for the Study of Arctic Climate) expedition to quantify the mass contribution of recrystallized sea ice to the Arctic snowpack. To understand and quantify the metamorphic processes of snow on sea ice, it is essential to combine our density and isotope measurements to make a case for this sea-ice-sourced snow. In particular, since the snow heterogeneity complicates the mass flux quantification from density changes, we also attempt to quantify how much the sea ice sublimates up into the overlying pack using an isotopic mixing model.

In this work, we use co-located in-situ measurements of snow temperatures, stable water isotopes, and snow density at specific areas, ~1m^2, obtained from excavated snow areas above the sea ice surface. We measured snow temperatures in snowpits using a needle thermometer inserted horizontally into the snow at 3 cm increments (including T_s and T_i). We calculated ΔT using the equation $\Delta T = (T_i - T_s)/h_s$. Isotopic snow samples were collected within the snowpits, in vertical profiles of 3 cm vertical resolution, and transported to the research vessel (RV) frozen in sealed pots. In total, 515 snow isotope samples were collected and analyzed. Two sampling methods were used, named SLF and CiASOM, throughout this manuscript. Details can be found in the isotope and salinity sample collection methods section. An overview of all isotopic profiles is shown in Fig. 1b. In addition to the stable water isotopes, the same samples were measured for conductivity to obtain salinity. The density of the snowpack was measured using primarily density cutter measurements, which obtained density by weighing a fixed volume of snow (100 cm^3) on an in situ scale with a 6% uncertainty, adapted from ref. 35. In addition, density was also measured using a desktop cone-beam microCT90 (microCT) installed in a laboratory onboard the RV Polarstern. This instrument allowed us to measure additional microstructural properties of the snow, e.g., anisotropy and specific surface area, which are not used in the main body of this study but are outlined in the supplementary information. The microCT samples and density cutter measurements were co-located with isotopic samples through cross-comparison of the height of the measurements. More details can be found in the methods section.

Results

Snow temperature gradients drive mass redistribution

During the MOSAiC expedition, the regional atmospheric winter conditions were normal relative to the preceding four decades, with a few anomalous synoptic events outlined in detail in ref. 36. In summary, an event in December had temperatures at the edge of the 95th percentile, and ranked as the fifth warmest period in the climatology, and a handful of events between late fall and early spring transported warm, moist air into the Arctic[36]. On the contrary, March had anomalous northerly winds bringing cold polar air into the region. Snow depth measurements revealed a shallower snowpack in this region, relative to other areas in the Arctic Basin[1,19]. These two conditions influence ΔT and the amount of TGM within the internal snowpack.

The ΔT values for each snowpit are shown in Fig. 2a against the measurement date. The average ΔT after calculating it for each snowpit was 61 K m^{-1} (standard deviation, σ = 52 K m^{-1}). The snow-ice interface temperature gradient is predominantly determined by the snow's thickness and thermal properties, dampening atmospheric temperature fluctuations. The snow generally has a stronger impact on the snow-ice interface temperature gradient than the sea ice thickness and the relatively stable ocean temperature. We therefore identify that the significant influence on the sea ice surface sublimation is the snow depth, and it is less significantly impacted by the sea ice thickness. Nonetheless, we agree that thicker sea ice would reduce the temperature gradient across the entire ice profile; however, as we are only interested in the interface, we continue to analyze our data relative to the snow depth. The mean snow depth (h_s) was 192 mm (σ = 158 mm) (within the 100–300 mm range obtained from the magnaprobe dataset[19]), and the average temperature was −17 °C (σ = 6 °C) from the snowpit temperature dataset. The large standard deviation of ΔT is due to varying h_s (seen on the x-axis in Fig. 2b) and late-winter atmospheric warm air intrusions from the mid-latitudes into the high Arctic, causing $\Delta T < 0$[37]. The transition between equilibrium fractionation and kinetic growth in the snow for different vapor pressure gradient thresholds (mbar/m) is visualized in Fig. 2c as outlined in ref. 38. Sixty-seven percent of the measured temperature gradients are in excess of the 5 mbar/m threshold required for kinetic-growth metamorphism to occur.

Quantification of mass redistribution

The upward vapor flux during snowpack TGM typically reduces the density of the lower snowpack and forms depth-hoar structures as a result of upward vapor transport along vapor pressure gradients[9]. One main driver of diffusion is the divergence of moisture flux caused by either a change in temperature gradient between the sea ice and the snow or a change in porosity between the sea ice and the snow[13]. identified a strong sublimation layer attached to the sea ice-snow interface with the largest negative change −66 kg m^{-3}.

We assume that all vapor from the underlying sea ice is taken up into the snowpack, and it is unlikely that warmer vapor will pass through the snow without deposition. Especially due to surface energy processes (e.g., longwave cooling) as the vapor reaching the snow surface from below will condense at or just below the cooler surface[39]. Nonetheless, it is important to note that there is also significant sublimation of the upper snowpack due to the moisture gradient with the atmosphere (dependent on air temperature, specific humidity of the

https://doi.org/10.1038/s41467-026-68762-0

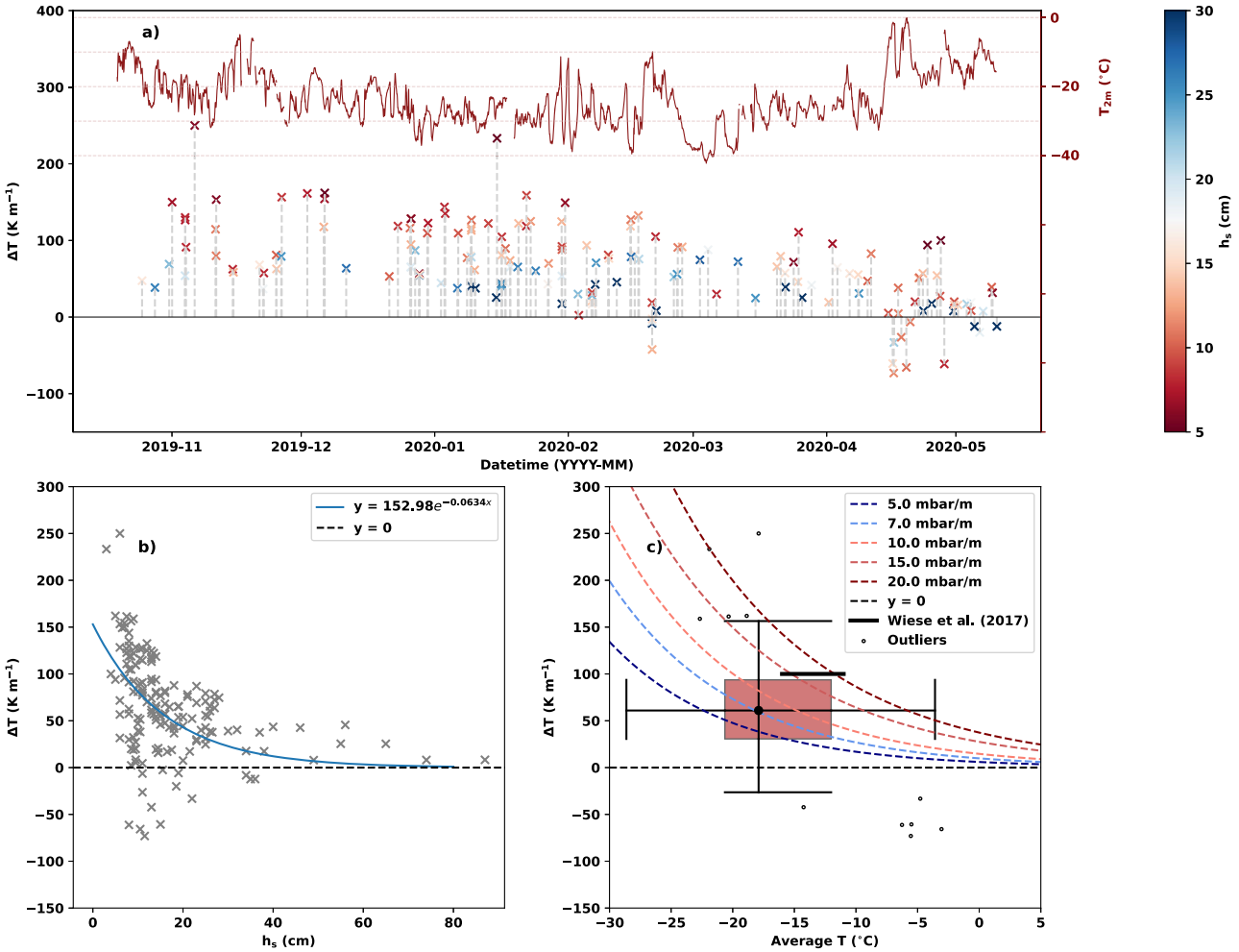

Fig. 2 | Snow temperature gradients (ΔT) measured in snowpits during the MOSAiC expedition between November 2019 and May 2020. ΔT is the surface temperature minus the snow-ice interface temperature, so $\Delta T > 0$ when the sea-ice interface (T_i) > snow surface temperature (T_s). This figure shows ΔT plotted **a** against the measurement date, showing that the strongest gradients were at the base of the snowpack and atmospheric temperature at 2 m (T_{2m}) over time (red), **b** relative to snowpit height, and **c** relative to the average snowpit temperature as a boxplot with data outliers shown as markers. The dotted lines represent vapor pressure gradient thresholds adapted from ref. 38, showing the transition between equilibrium fractionation and kinetic growth for any measurements above the 5 mbar/m plot.

air, surface temperature) and turbulent fluxes (i.e., higher with increased wind or higher roughness length). However, we focus on the mass lost from the snow-ice interface and have not attempted to estimate the mass sublimation from the snow surface.

Figure 3a shows the heterogeneity of the snow density cutter dataset, highlighting the complexity of the snowpack density and its limitations as a straightforward basis for estimating the mass contribution of recrystallized sea-ice snow. We can see by looking horizontally along the bottom of Fig. 3a that there was a systematic density reduction in the lower half of the snowpack after January 2020 (see samples at and below 0.4 on the *y* axis in Fig. 3a), implying upward vapor flux and mass re-distribution. In addition, mid- and upper-pack densities increased, in part due to wind slab development but perhaps also due to upwards mass deposition from below.[40] proposed that these low-permeable wind slabs could prevent convection, and ref. 13 confirmed that convection could occur in low-density snow (i.e., depth hoar), but once a dense layer of snow forms on top (i.e., wind compacted rounded grains), the convection process is halted. Due to the spatial heterogeneity, the analysis of these snow cutter density measurements was limited. Therefore, we compare the empirical relationship from the controlled laboratory study from ref. 24 given in Equation (1).

The laboratory snow density (201 kg m^{-3}) used by Wiese[24] was marginally lower than the average snow density in our study during the MOSAiC expedition (290 ± 34 kg m^{-3}). The 100 K m^{-1} temperature gradient and average snow temperature from ref. 24 is plotted in Fig. 2c as a horizontal black line, showing the high metamorphism rate of this experiment spanning the 15–20 mbar/m thresholds. This shows that the laboratory conditions are relative to the upper quartile of our measured conditions (93 K m^{-1}). Using the empirical relationship in Equation (1) from ref. 24, and multiplying ITE by the daily vapor pressure gradient ratios, as shown on the y-axis in Fig. 4, we can obtain an approximation for the sea ice sublimation. The ratios are calculated using the August-Roche-Magnus formula[41] to obtain the saturated vapor pressure over ice (see Equation 2), where e_s is in hPa, and T is in degrees Celsius. Calculations of e_s for each snowpit measurement are then used to obtain the vapor pressure difference at the snow surface and the snow-ice interface individually. The vapor pressure difference is then divided by the distance between the two measurements (i.e., the snow height) to estimate the vapor pressure gradient. The vapor pressure gradient ratio refers to the values relative to the laboratory experiment in ref. 24. We can use this method to estimate the sublimation of the ice surface between 25th October 2019 and 10th May 2020 (198 days). When multiple temperature gradients were measured on one day, an average was taken. If no measurements were taken, the seasonal average was used, indicated using a black cross in Fig. 4. 95 days had measurements, and the daily values were summed to give

https://doi.org/10.1038/s41467-026-68762-0

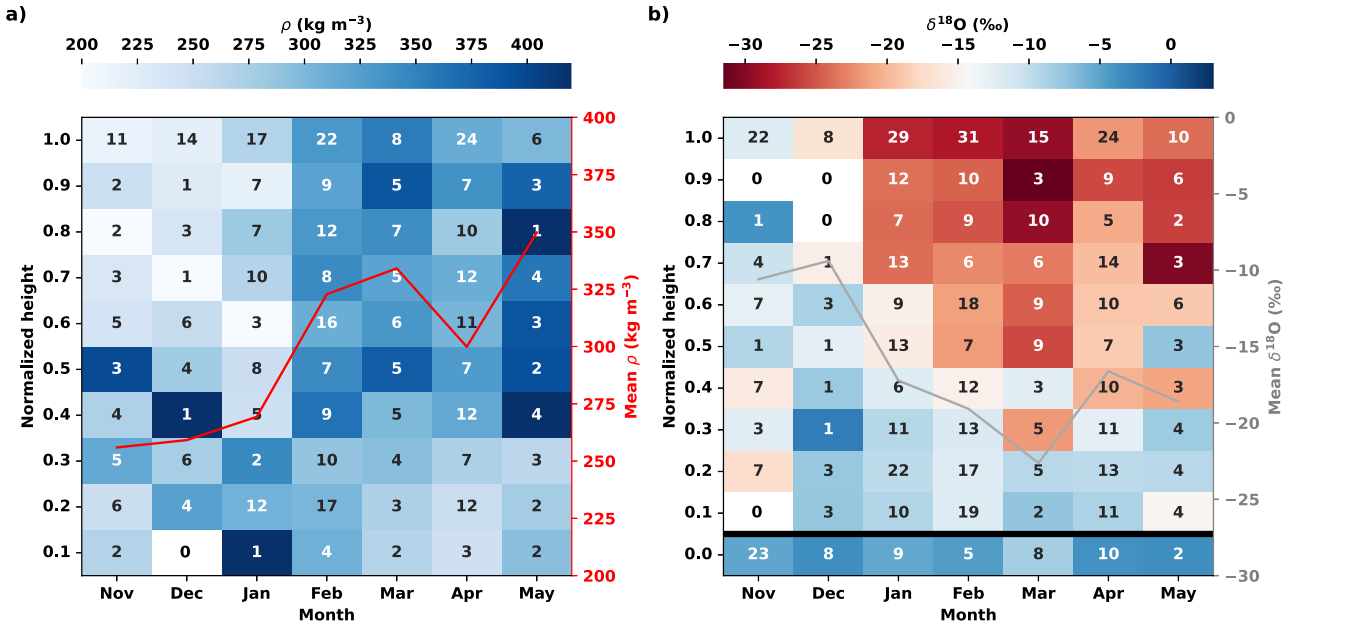

Fig. 3 | A figure linking density changes and isotopic enrichment of snow measured during the MOSAiC expedition. a A heatmap of height-normalized monthly density measured using the density cutter. The values within each cell show the number of measurements. The average monthly density values for all profiles are shown as a red curve, plotted on the secondary/right *y* axis. **b** A heatmap of height-normalized monthly averaged isotopic samples of $\delta^{18}O$. The values within each cell show the number of snow samples. The average monthly isotopic values are shown in the overlying gray, also plotted on the right *y* axis.

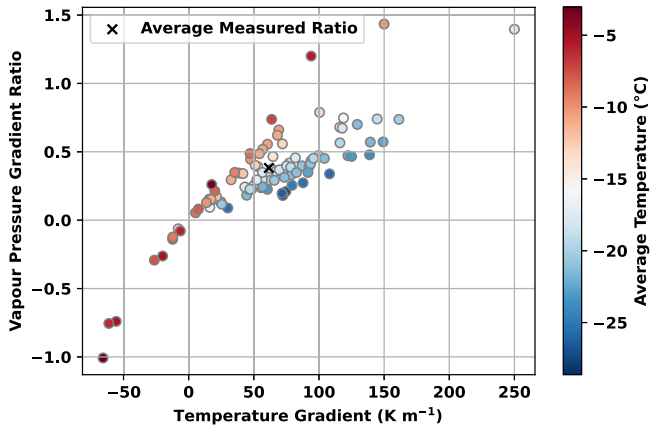

Fig. 4 | A figure showing the range of vapor pressure gradient ratios of each measured snowpit. The vapor pressure gradient ratios are calculated relative to the conditions found in Wiese et al. [24], plotted against temperature gradient and average snowpit temperature. These ratios were used to scale the estimated sublimated ice thickness equivalent for our study period. For days with no snowpit measurements, the seasonal average was used, indicated with a black cross.

the cumulative ITE. The remaining 103 days used the seasonal average. This resulted in a cumulative ITE of 13 mm, which can be converted to snow depth equivalent (SDE) by taking the average density of snow and ice as $\rho_s = 290 \pm 34\ \mathrm{kg\,m^{-3}}$ (see methods for details), and $\rho_i = 900 \pm 36\ \mathrm{kg\,m^{-3}}$, respectively. Applying Equation (3)[42], SDE = 39 ± 7 mm. The error is obtained from ref. 24, however, we acknowledge the large uncertainty in this method, which we discuss again in the discussion and implications section.

$$e_s(T) = 0.61094 \exp\left(\frac{17.625T}{243.04 + T}\right) \quad (2)$$

$$\mathrm{SDE} = \mathrm{ITE} \times \frac{\rho_i}{\rho_s} \quad (3)$$

Stable water isotope gradients in the lower snowpack

In all but four snow isotopic profiles, we found distinguishable signals of a) fresh snow precipitation in the upper layers of the snowpack and b) signals at the bottom of the snowpack that indicate it had undergone TGM. In general, measurements showed the average snow sample at the snow-ice interface was substantially more enriched in $\delta^{18}O$ (−11‰, $\sigma = 6$‰) than a surface snow sample in contact with the atmosphere (−33‰, $\sigma = 7$‰) and was closer to the $\delta^{18}O$ values of the sea-ice substrate (−4‰, $\sigma = 3$‰ for this study period). In Fig. 1b, a negative covariance (−6‰-cm) of the average $\delta^{18}O$ snow profile is shown.

We propose that this late-winter signal mainly originates from the sublimation of sea ice and vapor deposition into the snowpack above. The fractionation between ^{18}O and ^{16}O is represented by simple pie charts in Fig. 1a, showing phase transitions where heavy isotopes are less likely to make it into the vapor phase than the light isotopes, and the light isotopes are less likely to transfer into the solid phase. Since the sea ice is isotopically much heavier than snow[43], the empirical evidence suggests basal enrichment.

The lower snowpack was stable and unlikely to become completely eroded by wind. However, wind mixed and redistributed the upper snowpack, which caused an averaging effect on the isotopic composition of the surface snow, especially apparent in ridged areas[44]. The temporal evolution of the isotopic profiles (see Fig. 3b) and a few sampling sites with repeat measurements (see Supplementary Figure 1 from ref. 43) show that despite the snow's high spatial variability, this vertical gradient is apparent throughout winter. Although no observations of flooding or snow-ice were recorded in the MOSAiC central observatory[45], identified flooded areas in local depressions in close proximity to ridged areas, these processes would enrich the lower snowpack whilst simultaneously increasing the density to near-ice values. See the supplementary information on excluding flooding processes for further details.

In the literature, a second-order isotope parameter, deuterium-excess (d-excess = $\delta^2H - 8 \times \delta^{18}O$)[25], provides insights into i) the meteoric input defined by the primary moisture source conditions and ii) post-depositional processes within the snowpack[46]. For example,

https://doi.org/10.1038/s41467-026-68762-0

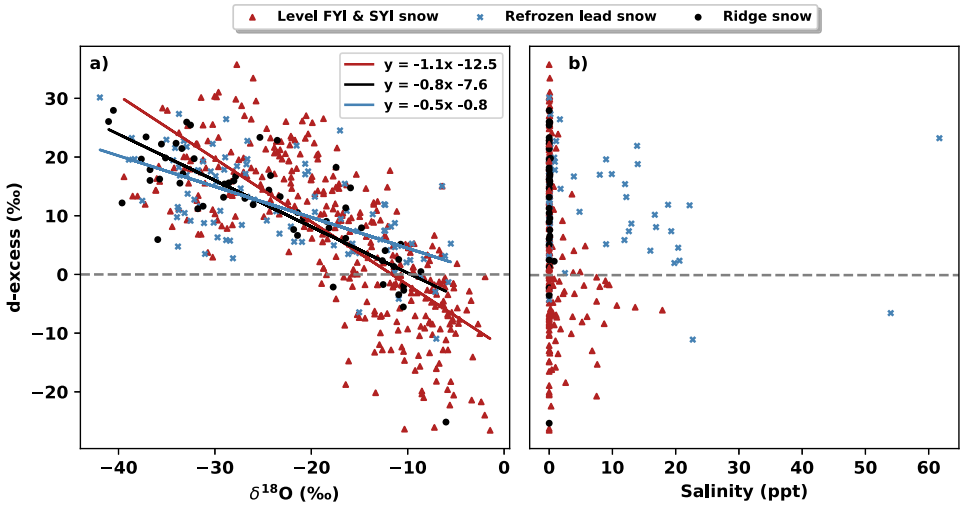

Fig. 5 | Second-order stable water isotope parameter, deuterium-excess, grouped by ice-type substrate, plotted for all winter snow samples. Deuterium-excess against **a** $\delta^{18}O$, and **b** salinity values. The colors in both plots indicate snow collected on level first-year (FYI) and second-year ice (SYI), refrozen leads, and ridged ice areas. Each marker in this figure is one snow sample collected between November 2019 and May 2020. **b** shows how saline samples on level ice are mainly associated with a negative d-excess signal, in contrast to snow on refrozen leads, where the saline samples have a positive d-excess signal. This indicates that d-excess could be used as a potential proxy for the amount of metamorphic recrystallization in saline snow on sea ice.

non-equilibrium fractionation processes during sublimation and re-sublimation can result in d-excess changes[47]. Our d-excess calculations revealed unexpectedly negative values close to the snow-ice interface, seen in Supplementary Figure 7. Between snow height 0–5 cm, the average d-excess equaled −1‰ (σ = 11‰), but single values as low as −27‰ were also measured. Snow at the surface had an average d-excess of 13.4‰ (σ = 5.4‰), and the sea-ice substrate had an average d-excess value of 0.8‰ (σ = 1.9‰[43]).

We use d-excess alongside conductivity salinity measurements to eliminate the possibility that the enriched isotope values were due to saline snow from processes such as sea spray deposition, brine-wicking (the movement of brine by capillary action), or frost flower inclusion processes. Each marker in Fig. 5b shows a snow sample's salinity (measured through conductivity) and isotopic d-excess. For this analysis, we separated our snow samples into the substrate types upon which they were collected using the categories: snow on level first-year ice (FYI) and second-year ice (SYI), snow on re-frozen leads, and snow in ridged areas. The distribution of the d-excess values for each ice type category can be seen in Fig. 5a plotted against $\delta^{18}O$. Figure 5b shows how saline snow is typically found on refrozen leads and level FYI and SYI snow areas. However, the difference between these samples can be seen with the isotope d-excess values. Excluding a few outliers, we see that younger, less-metamorphosed snow on refrozen leads typically has positive d-excess values, whereas more metamorphosed snow on level ice has the majority of negative d-excess values. The presence of salty snow with positive d-excess values shows that the above-mentioned processes, which lead to saline snow, typically do not result in decreasing d-excess values[43]. We hypothesize that there is a greater proportion of recrystallized sea-ice snow on level ice in contrast to the meteoric snow on re-frozen leads, and the negative d-excess values are likely to stem from complex metamorphic recrystallization processes at the snow-ice interface, leading to a disproportionate fractionation of δ^2H and $\delta^{18}O$.

Supplementary Figure 5 shows the deviation from the global meteoric water line in the lower samples (shown in red), causing this negative d-excess. In general, this is not a strong deviation and an argument that, in the first approximation, the isotopes can be used for two-component mixing calculations (see section below). Individual samples with very negative d-excess values indicate non-equilibrium kinetic fractionation beyond a two-component mixing model, where care is needed.

Quantifying isotopic enrichment with two-source endmembers

We used a two-source endmember approach of our isotopic measurements to quantify the contribution of recrystallized sea-ice snow. In the sea-ice environment, there is a clear differentiation of snow that has precipitated from the atmosphere (meteoric snow, $\delta^{18}O$ between −15‰ to −35‰[48–50]) and sea ice frozen from the ocean water (with second-year ice (SYI) $\delta^{18}O$ = −4.5‰ and first-year ice $\delta^{18}O$ = −0.7‰[43]). These two origins of snow (the atmosphere and sublimation from the sea ice) could be treated as two source endmembers[51]. Following the methods outlined in ref. 52, we used a mixing model and the endmember $\delta^{18}O$ signatures[53–56] to calculate the fraction of recrystallized sea-ice snow by mass, f_s, for each snowpit (Equation 4,[53]). The distribution of f_s values is visualized in Fig. 6, where δ_i is the average $\delta^{18}O$ value for sea ice (−4‰, σ = 3‰, n = 79 for this study period), δ_x is each snow profile's average $\delta^{18}O$, δ_s is the $\delta^{18}O$ value for meteorically precipitated snow, of which we used the surface snowpit snow sample. The two sample sets (CiASOM and SLF) were comparably taken, and we treat them both separately and combined, as shown in the three histograms in Fig. 6. This gives an average f_s of 0.33 (33 ± 9%, σ = 14 %) of recrystallized sea-ice snow. The error for CiASOM samples ± 0.1‰ and for the SLF samples ±0.5‰ gives an absolute error of 25% for each calculation of f_s; details of this calculation are given in the isotopic overview supplementary information.

$$f_s = \frac{\delta_x - \delta_s}{\delta_i - \delta_s} \tag{4}$$

An average snow height (h_s) of 192 ± 10 mm (σ = 158 mm, see the methods for details) corresponds to a recrystallized sea-ice SDE of 63 ± 21 mm (σ = 60 mm) (SDE = $h_s f_s$) and a SWE of 18 ± 7 mm (σ = 19 mm) (SWE = SDEρ_s, when ρ_s = 290 ± 17 kg m^{-3}, σ = 34 kg m^{-3}, using the 6% uncertainty given by Proksch et al.[35], and SDE in m). The large range of values for f_s in this calculation, and seen in Fig. 6, is due to the large σ of our isotope profiles (77 %), which can be attributed to snow heterogeneity through processes such as wind re-distribution. Values of f_s below 0 are where the surface snow is more enriched than the interface snow, typically occurring in thin snowpits reflecting the

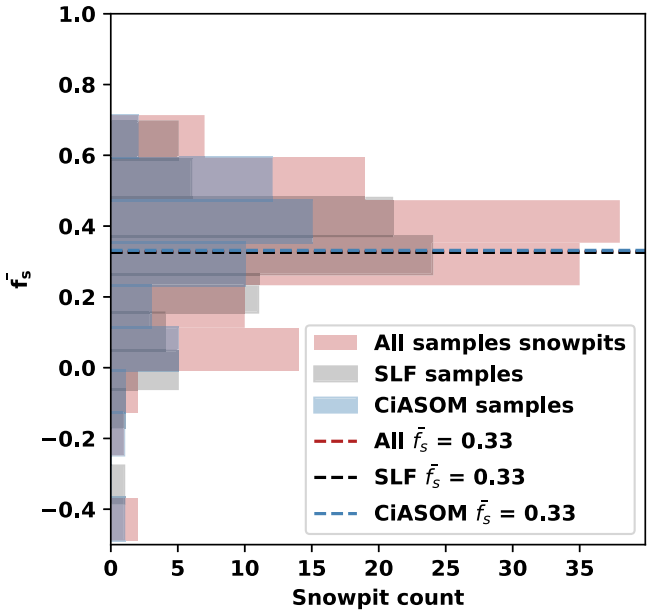

Fig. 6 | Histogram of the contribution of recrystallized sea-ice snow in the central Arctic winter. Quantifying the contribution of recrystallized sea-ice snow to each individual snowpit was calculated using the isotopic two-source end-member approach. f_s is the fraction of recrystallized sea-ice snow by mass for each isotopic profile collected in a single snowpit. The dataset has been split to show the two different sets of isotope samples (SLF and CiASOM), and the average recrystallized sea-ice snow contribution for winter is shown in the horizontal dotted lines.

high variability of snowpack in this region. In summary, isotopes suggest the sea ice contributed to the equivalent of a snow layer ~6 cm thick at the bottom of the snow.

Discussion

Our estimated contributions of recrystallized sea-ice-sourced snow should be used as a starting point for future discussion and improved modeling efforts in this domain.

Based on mass redistribution, a cumulative SDE of 39 ± 7 mm was obtained for the study period. The main uncertainties in this method come from the use of the August-Roche-Magnus approximation for the saturated vapor pressure and the 103 days of unknown temperature gradients in the snowpack, where we use the average winter temperature gradient instead. Future work implementing a physical model to investigate vapor fluxes through the snow under the conditions measured in this region is needed to compare with our estimations and reduce these quantification uncertainties. However, snowpack modeling is beyond the scope of this work.

The second method determines average isotopic enrichment from the underlying sea ice to be on average 63 ± 21 mm using an isotope two-source endmember approach. This second method neglects snow fractionation processes during metamorphism, which enriches the snow in $\delta^{18}O$ (in the range of 5 ‰[27]), causing an overestimation. However, wind homogenization would mix the isotopically depleted meteoric snow, causing an underestimation of the recrystallized sea-ice contribution of an unknown amount.

At the beginning of the season, the snow's isotopic enrichment at the interface is less apparent and this is likely due to a number of processes (1) the wind redistribution and mixing of the snowpack before it has sintered, this prevents the preservation of atmospheric precipitation events in the snowpack stratigraphy, and (2) spatial and temperature influences in the precipitation's isotopic signal. This latter can be addressed by building on the work of ref. 37, who investigates the atmospheric water vapor isotopic signal throughout the expedition. We assume precipitated snow follows the isotopic trends of the atmospheric vapor. This atmospheric water vapor was also depleted at the start of the season (likely because it is already quite cold and far from the ice edge) and remains reasonably stable between November 2019 and April 2020, excluding the warm air intrusion events, which bring enriched isotopic vapor. However, these intrusions may cause transient enrichment but are not frequent or sustained enough to explain a systematic enrichment at the snowpack base[57] showed that these warm air intrusions do not always align with enriched snowfall. Unfortunately, we did not explicitly collect fresh snow samples for isotopic analysis, and due to large amounts of snow mixing, the fresh snow isotopic signature was hard to disentangle. Finally, the negative d-excess values would not be obtained simply from the accumulation of early-season $\delta^{18}O$-enriched snow, implying that another process must come into play. Persistent negative d-excess values indicate post-depositional modification (e.g., sublimation), which preferentially removes heavy isotopes and further depletes the remaining snow.

The isotopic samples grouped by normalized height in Fig. 3 need to be interpreted with care, as we also have deepening snow over the season. This could be why we do not see a continuously enriching snowpack. Over time, the snowpack becomes more stable and compact, resulting in less mixing of the entire snowpack. As a result, the late-season upper snowpack is likely to be less influenced by the recrystallized sea ice and more by the atmospheric deposition, creating the apparent upper and lower snowpit differentiation of their isotopic signatures. We also see this with the snow stratigraphy, as we have a lower depth hoar layer (likely with more sea-ice sourced snow) and an upper wind slab layer forming over the season (with more atmospheric snow). While it is important to note that the largest uncertainty for snow accumulation on Arctic sea ice is wind redistribution, we show that a high proportion of the snow depth may originate from recrystallized sea-ice snow. This general understanding has implications for snow mass balance estimates, gas flux, light transmission, and heat flux estimates in the Arctic.

Stable water isotopes have proven valuable in showing that there is likely to be substantial recrystallization of the sea ice contributing to the snowpack enrichment; however, calculations of the contribution are uncertain using this method. For this reason, future work using a combined physical and isotopic model is needed to compare with our estimations, similar to the work done by Touzeau et al.[32], bridging the vapor diffusion with isotope modeling. However, this is beyond the scope of this work.

To test our calculations, we compare our study to snow TGM at tundra sites. The work by Sturm[20] suggests 2–5 mm SWE enter the base of the snow from the soil in 150 days. Less vapor is likely to be provided by a tundra substrate compared to a sea-ice substrate, as vapor from ice is not trapped in between the soil structure. Additionally, as the soil sources moisture, the surface soil desiccates, leading to the ice source being deeper in the ground, which further inhibits upward mass transfer. This supports our larger estimates of recrystallized sea ice snow in the sea-ice environment. This also agrees with Wiese's[24] approximation of ice mass flux being approximately four times larger than Sturm's[20], likely because of the larger ice surface area for sublimation. These study values are provided in the introduction. To conclude, we expect greater availability of vapor from an ice substrate compared to a porous soil substrate.

Our measurement in a shallower snowpack (relative to other areas in the Arctic Basin[1,19]) with higher ΔT have experienced more metamorphism, increased isotope enrichment in heavy isotopes, and as a result, we are likely to overestimate the SWE contribution. Nonetheless, sea-ice recrystallization is a general process of the sea-ice domain, and any snow on sea ice that is exposed to a positive temperature gradient has the potential to incorporate mass from the sea-ice substrate. Snow on sea ice in Antarctica is expected to undergo the same process under comparable snow and sea-ice conditions; however, the thicker the snow cover, the smaller the SWE contribution.

Alternative processes also come into play in Antarctica, for example, in some areas, a persistent snowpack from the previous years is present on the sea ice. Additionally, our study excludes flooding processes (See the supplementary information on excluding flooding processes), however in Antarctica, flooding processes need more consideration due to increased precipitation.

This study does not explore impurity origins in the snowpack, but notes that recrystallized sea ice contributes mass to the snowpack and, as a result, the impurity concentration in the snow may progressively dilute[58,59] throughout the winter. These impurities refer to black carbon[59], soluble ions (e.g., ammonium;[60]), and natural minerals (e.g., salts and dust)[61]. Alternatively, impurities (e.g., salt and halogens) could be made more available to atmospheric transport, as ions with high ice solubility can be incorporated into the ice interior and relocated during recrystallization[60,61]. TGM and sea-ice-sourced snow will influence snow depth, snow density, specific surface area, grain size and potentially sea-salt distributions in the snowpack; understanding this is critical to improving our understanding of remote seeing backscatter signals with altimetry applications[62]. Finally, the vertical distribution of snowpack impurities will become increasingly critical in Arctic warming during wind-redistribution and blowing snow events[63], where the snowpack acts as a source of atmospheric aerosols[64], trace gases[65], and other chemical compounds like bromine and molecular iodine[66], which contribute to Arctic ozone destruction and gaseous mercury[67,68].

Central Arctic climatic predictions point towards substantial regional differences in precipitation[69]. Regions with thicker snowpacks will have smaller ΔT, resulting in less metamorphism and recrystallized sea-ice snow. This has the potential to reduce the dilution of impurities. Other regions with reductions in snow accumulation would have increased gas fluxes through the snow to the atmosphere, alongside changes in light transmission to the ocean[63] and thermal conductivity of the snowpack. This process could have implications for climate modeling, and future work improving the representation of this process could benefit Earth system models. In summary, this improved understanding of the mass contribution from recrystallized sea-ice snow could help disentangle the intricate snow-sea ice system and its trajectories.

Methods

This manuscript studies snow on sea ice in the winter months from November 2019 to May 2020 (therefore excluding melt influences) in the high Arctic between 83.4°N and 88.6°N. During the MOSAiC expedition, the RV Polarstern drifted within the Arctic pack ice, allowing repeat measurements of a single ice floe. In total, three ice floes were studied throughout the whole expedition; however, this study only investigates the first, named Central Observatory 1 (CO1), between October 2019 and May 2020. This ice floe had a diameter of ~1 km. Five aspects of the system were investigated, including the atmosphere, ocean, sea ice (and snow), ecosystem, and biogeochemistry. To describe the evolution of the snowpack conditions over time, snowpit sites were set up and marked with flags on the ice floe, which were designated locations assigned to repeat in situ snow measurements. A time series of the snowpack's physical (e.g., structural), (isotope) geochemical, and salinity development was constructed by repeatedly visiting the same measurement locations and following the same measurement protocols. The snowpit sites were returned to weekly or bi-weekly unless ice dynamics meant they were inaccessible. The snowpit sites were chosen randomly. However, the measurer ensured snowpit sites included a selection of ice substrate conditions, including level first-year ice and second-year ice areas, leads, and ridges. A snowpit event was one trip to the ice and included a library of different snow measurements measured simultaneously; the events are labeled in the format PS122/"Leg#"_"Week#"-"UniqueID", e.g., PS122/2_19-92[70]. The measurements conducted during one snowpit event depended on the time and ice conditions on the given day. In all, 128 snowpits are included in this analysis. More details on the data collection methods, data storage, and format can be found in the following sections, the published datasets[70] and the online data paper[71].

Density and SSA as a function of height

Snow microstructural measurements were taken within the snowpits alongside the snow height[72], isotope and salinity profiles. The density cutter was used to obtain the data used for Fig. 3a. This measurement measures the weight of 100 cm^3 of snow in situ on calibrated weighing scales. The density cutter was used to take vertical profiles of snow samples every 3 cm.

To obtain more detailed microstructural measurements, we also used a microCT[73]. This could measure density at high vertical resolution, specific surface area, and provide details on snowpack anisotropy. We used the microCT data to obtain data for Supplementary Figure 8. Analysis with the microCT requires snow samples to be collected in the field, transported to the Polarstern, and measured using the microCT. The microCT has a resolution of 22 µm. MicroCT profiles are publicly accessible on Pangaea[73]. The ice and air volumes were separated to obtain profiles of density. SSA was calculated using the triangular-based total surface area of snow per unit mass (with units of $m^2\,kg^{-1}$) of sub-volumes within the snow samples. Geometric anisotropy is defined in this manuscript by the relationship outlined in Equation (5), in terms of the correlation lengths ξ in different coordinate directions x, y, z. The correlation lengths were obtained by fitting the decay of the two-point correlation function in different directions to an exponential[74]. These parameters are used for Supplementary Figure 8.

$$A_g = \frac{2\xi_z}{\xi_x + \xi_y} \tag{5}$$

Samples of isotope and salinity as a function of height

Isotopic snow samples were collected within the snowpits, in vertical profiles in the field, and transported to the RV Polarstern in sealed pots. In total, 515 snow isotope samples were collected and analyzed later in two laboratories (The Swiss Federal Research Institute WSL and the ISOLAB Facility at the Alfred Wegener Institute Helmholtz Center for Polar and Marine Research in Potsdam, Germany) for the study period between November 2019 and May 2020. Both datasets contribute to this manuscript. The first dataset[75], named SLF, took vertical profiles of snow samples (each 100 cm^3). The vertical resolution of these samples was every 3 cm. After the samples were transported to RV Polarstern, the samples were melted for salinity measurements (using the YSI 30 Salinity, Conductivity and Temperature sensor,[76]). These samples were sealed into 20 ml glass vials onboard Polarstern. Each sample was then transported to Switzerland and measured for stable water isotopic composition at WSL, Zurich, using a Los Gatos Research (LGR) Isotopic Water Analyzer (model IWA-45EP) instrument. Each sample was measured five times in this dataset,[75] with a resulting measurement accuracy of $\delta^{18}O \pm 0.5‰$ and $\delta^{2}H \pm 1‰$. The second dataset, named CiASOM, was collected in the snowpit at three layers: top, middle, and bottom. A plastic shovel was used to sample the snow in these three layers directly into plastic bags. These samples were transported to RV Polarstern and remained frozen onboard as they were stored at −4 °C. After the expedition, this second dataset was sent to AWI, Germany, thawed at room temperature, poured into 20 ml glass vials, sealed with parafilm tape, and stored at 4 °C. This dataset was measured for stable water isotopes using mass spectrometers (DELTA-S Finnigan MAT, USA) using equilibration techniques to an accuracy of better than ± 0.1‰ for $\delta^{18}O$ and ± 0.8‰ for $\delta^{2}H$. Every sample is equilibrated and then transferred to the Isotope Ratio Mass Spectrometry, where it is measured 10 times against a standard of known isotope composition. The statistics of one single datapoint are

based on these ten measurements. Both datasets are published with open access in Pangaea, where more details can be found.

Sea ice samples were collected during ice coring events using a Kovacs Mark II 9 cm diameter corer from ice of differing ages. The snow on top of the sea ice was brushed off the top of the cores to minimize snow affecting the ice surface. More details on the sampling and measurement methods are outlined in Section 2.2.2. in ref. 43.

A comparison was conducted between the two laboratories by measuring fifty samples twice to show continuity between the datasets. The fifty selected samples primarily originated from snow measurements on level ice with a range of isotopic signatures (see Supplementary Figure 2), but included a selection of samples with negative d-excess values. This negative d-excess was consistently observed in both datasets. It was found that the WSL-measured samples needed a correction due to evaporative fractionation during sample storage. The correction was done by calculating the mean of this dataset relative to the mean of the parallel dataset from AWI and correcting for the difference. This was possible as the histograms for both datasets were of a similar shape but appeared to have a shift, see Supplementary Figure 3. As a result, the $\delta^{18}O$ was corrected by −6.4‰, the $\delta^{2}H$ was corrected by −36.4‰, visualized in Supplementary Figure 4. Despite this correction factor, the enrichment signal analyzed in this study was apparent in both datasets, however, as mentioned in the main text, d-excess calculations need interpreting with care for the SLF dataset, as done in this study.

Data availability

The snowpit data generated in this study have been deposited in the Pangaea database accessible at https://doi.org/10.1594/PANGAEA.935934[70], this dataset includes snow temperature accessible at https://doi.org/10.1594/PANGAEA.940200[77], snow height accessible at https://doi.org/10.1594/PANGAEA.940215[72], and stable water isotope data measured at WSL accessible at https://doi.org/10.1594/PANGAEA.952556[75]. The AWI measured isotope data is available at https://doi.org/10.1594/PANGAEA.948511[57].

References

1. Webster, M. et al. Snow in the changing sea-ice systems. *Nat. Clim. Change* **8**, 946–953 (2018).
2. Giddings, J. C. & LaChapelle, E. The formation rate of depth hoar. *J. Geophys. Res.* **67**, 2377–2383 (1962).
3. de Quervain, M. Snow structure, heat, and mass flux through snow. in *The Role of Snow and Ice in Hydrology* 203–226 (IAHS-AISH Publ. 107, 1973).
4. Sturm, M. & Benson, C. S. Vapor transport, grain growth and depth-hoar development in the subarctic snow. *J. Glaciol.* **43**, 42–59 (1997).
5. Sturm, M., Holmgren, J. & Perovich, D. K. Winter snow cover on the sea ice of the arctic ocean at the surface heat budget of the arctic ocean (sheba): temporal evolution and spatial variability. *J. Geophys. Res. Oceans* **107**, SHE–23 (2002).
6. Dou, T. & Xiao, C. Measurements of physical characteristics of summer snow cover on sea ice during the third chinese arctic expedition. *Sci. Cold Arid Reg.* **5**, 309–315 (2013).
7. Merkouriadi, I. et al. Winter snow conditions on arctic sea ice north of svalbard during the norwegian young sea ice (n-ice2015) expedition. *J. Geophys. Res. Atmos.* **122**, 10–837 (2017).
8. Ji, Q., Pang, X., Zhao, X. & Lei, R. Snow features on sea ice in the western arctic ocean during summer 2016. *Int. J. Digit. Earth* **14**, 1397–1410 (2021).
9. Trabant, D. & Benson, C. Field experiments on the development of depth hoar. *Geol. Soc. Am. Mem.* **135**, 309–322 (1972).
10. Johnson, J. B., Sturm, M., Perovich, D. K. & Bens, C. Field observations of thermal convection in a subarctic snow cover. *Int. Assoc. Hydrol. Sci. Publ.* **162**, 105–118 (1987).
11. Alley, R., Saltzman, E., Cuffey, K. & Fitzpatrick, J. Summertime formation of depth hoar in central greenland. *Geophys. Res. Lett.* **17**, 2393–2396 (1990).
12. Sturm, M. & Johnson, J. Natural convection in the subarctic snow cover. *J. Geophys. Res. Solid Earth* **96**, 11657–11671 (1991).
13. Jafari, M. et al. The impact of diffusive water vapor transport on snow profiles in deep and shallow snow covers and on sea ice. *Front. Earth Sci.* **8**, 249 (2020).
14. Pinzer, B., Schneebeli, M. & Kaempfer, T. Vapor flux and recrystallization during dry snow metamorphism under a steady temperature gradient as observed by time-lapse micro-tomography. *Cryosphere* **6**, 1141–1155 (2012).
15. Calonne, N., Flin, F., Geindreau, C., Lesaffre, B. & Rolland du Roscoat, S. Study of a temperature gradient metamorphism of snow from 3-d images: time evolution of microstructures, physical properties and their associated anisotropy. *Cryosphere* **8**, 2255–2274 (2014).
16. Jordan, R. *A one-dimensional temperature model for a snow cover: Technical documentation for SNTHERM.89*. Special Report 91-16 (US Army CRREL, 1991).
17. Domine, F., Taillandier, A.-S. & Simpson, W. R. A parameterization of the specific surface area of seasonal snow for field use and for models of snowpack evolution. *J. Geophys. Res. Earth Surf.* **112**, F02031 (2007).
18. Filhol, S. & Sturm, M. Snow bedforms: a review, new data, and a formation model. *J. Geophys. Res.: Earth Surf.* **120**, 1645–1669 (2015).
19. Itkin, P. et al. Sea ice and snow characteristics from year-long transects at the mosaic central observatory. *Elementa: Sci. Anthropocene* **11**, 00048 (2023).
20. Sturm, M. *The role of thermal convection in heat and mass transport in the subarctic snow cover*. CRREL Report 91–19 (1991).
21. Flin, F. & Brzoska, J.-B. The temperature-gradient metamorphism of snow: vapour diffusion model and application to tomographic images. *Ann. Glaciol.* **49**, 17–21 (2008).
22. Bouvet, L., Calonne, N., Flin, F. & Geindreau, C. Heterogeneous grain growth and vertical mass transfer within a snow layer under a temperature gradient. *Cryosphere* **17**, 3553–3573 (2023).
23. Adams, E. E. & Miller, D. A. Ice crystals grown from vapor onto an orientated substrate: application to snow depth-hoar development and gas inclusions in lake ice. *J. Glaciol.* **49**, 8–12 (2003).
24. Wiese, M. Time-lapse tomography of mass fluxes and microstructural changes in snow. PhD thesis, ETH Zurich (2017).
25. Dansgaard, W. Stable isotopes in precipitation. *Tellus* **16**, 436–468 (1964).
26. Moser, H. & Stichler, W. Deuterium and oxygen-18 contents as an index of the properties of snow covers. *IAHS-AISH Publ.* **114**, 122–135 (1975).
27. Friedman, I., Benson, C. S. & Gleason, J. D. Isotopic changes during snow metamorphism. in *Stable Isotope Geochemistry: A Tribute to Samuel Epstein* (eds. Taylor, H. P. Jr., O'Neil, J. R. & Kaplan, I. R.) 211–221 (The Geochemical Society, 1991).
28. Sommerfeld, R. A., Friedman, I. & Nilles, M. The fractionation of natural isotopes during temperature gradient metamorphism of snow. in *Seasonal Snowcovers* (eds. Jones, H. G. & Orville-Thomas, W. J.) 95–105 (Springer, 1987).
29. Beria, H. et al. Understanding snow hydrological processes through the lens of stable water isotopes. *Wiley Interdiscip. Rev. Water* **5**, e1311 (2018).
30. Claassen, H. & Downey, J. A model for deuterium and oxygen 18 isotope changes during evergreen interception of snowfall. *Water Resour. Res.* **31**, 601–618 (1995).
31. Friedman, I., Smith, G. I., Gleason, J. D., Warden, A. & Harris, J. M. Stable isotope composition of waters in southeastern california 1. modern precipitation. *J. Geophys. Res. Atmos.* **97**, 5795–5812 (1992).

32. Touzeau, A., Landais, A., Morin, S., Arnaud, L. & Picard, G. Numerical experiments on vapor diffusion in polar snow and firn and its impact on isotopes using the multi-layer energy balance model crocus in surfex v8.0. *Geosci. Model Dev.* **11**, 2393–2418 (2018).
33. Ebner, P. P., Steen-Larsen, H. C., Stenni, B., Schneebeli, M. & Steinfeld, A. Experimental observation of transient δ 18 o interaction between snow and advective airflow under various temperature gradient conditions. *Cryosphere* **11**, 1733–1743 (2017).
34. Stuart, R. H. et al. Exploring the role of snow metamorphism on the isotopic composition of the surface snow at eastgrip. *Cryosphere* **17**, 1185–1204 (2023).
35. Proksch, M., Rutter, N., Fierz, C. & Schneebeli, M. Intercomparison of snow density measurements: bias, precision, and vertical resolution. *Cryosphere* **10**, 371–384 (2016).
36. Rinke, A., Cassano, J. J., Cassano, E. N., Jaiser, R. & Handorf, D. Meteorological conditions during the mosaic expedition: normal or anomalous? *Elem. Sci. Anth.* **9**, 00023 (2021).
37. Brunello, C. et al. Moisture transformation in warm air intrusions into the arctic: process attribution with stable water isotopes. *Geophys. Res. Lett.* **51**, e2024GL111013 (2024).
38. Armstrong, R. L. Some observations on snowcover temperature patterns. *Natl. Res. Counc. Can. Assoc. Comm. Geotech. Res. Tech. Memo.* **133**, 66–81 (1981).
39. Nyberg, A. Temperature measurements in an air layer very close to a snow surface. *Geogr. Ann.* **20**, 234–275 (1938).
40. Domine, F. et al. Soil moisture, wind speed and depth hoar formation in the arctic snowpack. *J. Glaciol.* **64**, 990–1002 (2018).
41. Alduchov, O. A. & Eskridge, R. E. Improved Magnus form approximation of saturation vapor pressure. *J. Appl. Meteorol.* **35**, 601–609 (1996).
42. Tian, L. et al. Stable isotope clues to the formation and evolution of refrozen melt ponds on arctic sea ice. *J. Geophys. Res. Oceans* **123**, 8887–8901 (2018).
43. Mellat, M. et al. Isotopic signatures of snow, sea ice, and surface seawater in the central Arctic Ocean during the MOSAiC expedition. *Elem. Sci. Anth.* **12**, 00010 (2024).
44. Mellat, M. et al. Arctic surface snow interactions with the atmosphere: spatio-temporal isotopic variability during the mosaic expedition. *EGUsphere* **2024**, 1–36 (2024).
45. Lei, R. et al. Seasonality and timing of sea ice mass balance and heat fluxes in the arctic transpolar drift during 2019–2020. *Elem. Sci. Anth.* **10**, 000089 (2022).
46. Madsen, M. V. et al. Evidence of isotopic fractionation during vapor exchange between the atmosphere and the snow surface in greenland. *J. Geophys. Res. Atmos.* **124**, 2932–2945 (2019).
47. Craig, H. & Gordon, L. I. Deuterium and oxygen 18 variations in the ocean and the marine atmosphere. in *Stable Isotopes in Oceanographic Studies and Paleotemperatures* (ed. Tongiorgi, E.) 9–130 (Consiglio Nazionale delle Ricerche, 1965).
48. Ala-aho, P. et al. Arctic snow isotope hydrology: a comparative snow-water vapor study. *Atmosphere* **12**, 150 (2021).
49. Levasseur, S., Brown, K., Langlois, A. & McLennan, D. Measurement of snow physical properties and stable isotope variations in the canadian sub-arctic and arctic snowpack. *Atmosphere-Ocean* **59**, 137–151 (2021).
50. Zuhr, A. M. et al. A snapshot on the buildup of the stable water isotopic signal in the upper snowpack at eastgrip on the greenland ice sheet. *J. Geophys. Res. Earth Surf.* **128**, e2022JF006767 (2023).
51. Lange, B. A. et al. Snowmelt contribution to Arctic first-year ice ridge mass balance and rapid consolidation during summer melt. *Elem. Sci. Anth.* **11**, 00037 (2023).
52. Lange, B. A. et al. Contribution of snow to arctic first-year and multi-year sea ice mass balance within the last ice area. *J. Geophys. Res. Oceans* **126**, e2020JC016971 (2021).
53. Jeffries, M. O., Shaw, R. A., Morris, K., Veazey, A. L. & Krouse, H. R. Crystal structure, stable isotopes (δ18o), and development of sea ice in the ross, amundsen, and bellingshausen seas, antarctica. *J. Geophys. Res. Oceans* **99**, 985–995 (1994).
54. Jeffries, M., Morris, K., Weeks, W. & Worby, A. Seasonal variations in the properties and structural composition of sea ice and snow cover in the bellingshausen and amundsen seas, antarctica. *J. Glaciol.* **43**, 138–151 (1997).
55. Granskog, M. A., Martma, T. A. & Vaikmäe, R. A. Development, structure and composition of land-fast sea ice in the northern baltic sea. *J. Glaciol.* **49**, 139–148 (2003).
56. Granskog, M. A. et al. Snow contribution to first-year and second-year arctic sea ice mass balance north of svalbard. *J. Geophys. Res. Oceans* **122**, 2539–2549 (2017).
57. Mellat, M. et al. Stable water isotopes of snow during MOSAiC expedition. *PANGAEA* https://doi.org/10.1594/PANGAEA.948511 (2022).
58. Doherty, S., Warren, S., Grenfell, T., Clarke, A. & Brandt, R. Light-absorbing impurities in arctic snow. *Atmos. Chem. Phys.* **10**, 11647–11680 (2010).
59. Flanner, M., Liu, X., Zhou, C., Penner, J. E. & Jiao, C. Enhanced solar energy absorption by internally-mixed black carbon in snow grains. *Atmos. Chem. Phys.* **12**, 4699–4721 (2012).
60. Trachsel, J. C. et al. Microscale rearrangement of ammonium induced by snow metamorphism. *Front. Earth Sci.* **7**, 194 (2019).
61. Hagenmuller, P. et al. Motion of dust particles in dry snow under temperature gradient metamorphism. *Cryosphere* **13**, 2345–2359 (2019).
62. Nandan, V. et al. Effect of snow salinity on cryosat-2 arctic first-year sea ice freeboard measurements. *Geophys. Res. Lett.* **44**, 10–419 (2017).
63. Lannuzel, D. et al. The future of arctic sea-ice biogeochemistry and ice-associated ecosystems. *Nat. Clim. Change* **10**, 983–992 (2020).
64. GGong, X. et al. Arctic warming by abundant fine sea salt aerosols from blowing snow. *Nat. Geosci.* **16**, 768–774 (2023).
65. Bartels-Rausch, T. et al. Ice structures, patterns, and processes: a view across the icefields. *Rev. Mod. Phys.* **84**, 885–944 (2012).
66. Marelle, L. et al. Implementation and impacts of surface and blowing snow sources of arctic bromine activation within wrf-chem 4.1. 1. *J. Adv. Model. Earth Syst.* **13**, e2020MS002391 (2021).
67. Pratt, K. A. et al. Photochemical production of molecular bromine in arctic surface snowpacks. *Nat. Geosci.* **6**, 351–356 (2013).
68. Benavent, N. et al. Substantial contribution of iodine to Arctic ozone destruction. *Nat. Geosci.* **15**, 770–773 (2022).
69. Webster, M., DuVivier, A., Holland, M. & Bailey, D. Snow on arctic sea ice in a warming climate as simulated in cesm. *J. Geophys. Res. Oceans* **126**, e2020JC016308 (2021).
70. Macfarlane, A. R. et al. Snowpit raw data collected during the MOSAiC expedition. *PANGAEA* https://doi.org/10.1594/PANGAEA.935934 (2021).
71. Macfarlane, A. R. et al. Author correction: a database of snow on sea ice in the Central Arctic collected during the MOSAiC expedition. *Sci. Data* **10**, 500 (2023).
72. Macfarlane, A. R. et al. Snowpit height measurements during the MOSAiC expedition. *PANGAEA* https://doi.org/10.1594/PANGAEA.940215 (2022).
73. Macfarlane, A. R. et al. MicroCT density and specific surface area snowpit profiles during the MOSAiC expedition. *PANGAEA* https://doi.org/10.1594/PANGAEA.952794 (2022).
74. Löwe, H., Riche, F. & Schneebeli, M. A general treatment of snow microstructure exemplified by an improved relation for thermal conductivity. *Cryosphere* **7**, 1473–1480 (2013).
75. Macfarlane, A. R. et al. Snowpit stable isotope profiles during the MOSAiC expedition. *PANGAEA* https://doi.org/10.1594/PANGAEA.952556 (2022).

76. Macfarlane, A. R. et al. Snowpit salinity profiles during the MOSAiC expedition. *PANGAEA* https://doi.org/10.1594/PANGAEA.946807 (2022).
77. Macfarlane, A. R. et al. MicroCT density and specific surface area snowpit profiles during the MOSAiC expedition. *PANGAEA*https://doi.org/10.1594/PANGAEA.940200 (2022).

Acknowledgements

We would like to acknowledge the time spent and the care taken by the AWI and WSL laboratories when conducting the stable water isotopic analysis of all the snow and ice samples. We thank and acknowledge Mareike Wiese for providing the microCT images presented in Fig. 1. Datasets used in this manuscript were produced as part of the international Multidisciplinary Drifting Observatory for the Study of the Arctic Climate (MOSAiC) with the tag MOSAiC20192020 and the Project_ID: AWI_PS122_00. We thank all the people involved in the expedition of the RV Polarstern during MOSAiC in 2019–2020 as listed at https://doi.org/10.5281/zenodo.5541624. We would like to thank Scanco Medical AG for lending and supporting the use of the MicroCT90 throughout the MOSAiC expedition. This work was possible due to the funding received by The Swiss Polar Institute (SPI reference DIRCR-2018-003), Funder ID: https://doi.org/10.13039/501100015594. European Union's Horizon 2020 research and innovation program projects ARICE (grant 730965) for berth fees associated with the participation of the DEARice project. WSL Institute for Snow and Avalanche Research SLF. WSL_201812N1678. Funder ID: https://doi.org/10.13039/501100015742. ARM received funding from the Swiss National Science Foundation (SNSF) project number P500PN_217845. SA received funding through the German Research Foundation's (DFG) projects fAntasie (AR1236/3-1) and SnowCast (AR1236/1-1) within its priority program "Antarctic Research with comparative investigations in the Arctic ice areas" (SPP1158), the DFG Emmy Noether Program project SNOWflAke (project number 493362232), and the Alfred Wegener-Institut, Helmholtz-Zentrum für Polar- und Meeresforschung. M.M., CFB, MW, and HM are grateful for the support provided by the German Federal Ministry of Education and Research (project MOSAiC-CiASOM, grant number 03FO869A).

Author contributions

A.R.M., M.M. and M.Sc. devised the study. A.R.M. managed the research, conducted the investigation, data analysis and wrote the original draft. A.R.M., M.M., H.M., C.F.B., M.W., R.D., and M.Sc processed the data. A.R.M., S.A., D.K., and M.Sc. were data curators. A.R.M., M.J. and N.W. worked on the quantification methods. A.R.M., M.M., H.M., C.F.B., M.W., R.D., S.A., D.K., M.Sc., M.St., M.J. and N.W. critically revised the manuscript for important intellectual content and approved the final version to be published.

Competing interests

The authors declare no competing interests.

Additional information

Supplementary information The online version contains supplementary material available at https://doi.org/10.1038/s41467-026-68762-0.

Correspondence and requests for materials should be addressed to Amy R. Macfarlane.

Peer review information *Nature Communications* thanks the anonymous reviewers for their contribution to the peer review of this work. A peer review file is available.